Journal of Materials Chemistry A

PAPER

View Article Online
View Journal | View Issue

Cite this: J. Mater. Chem. A, 2019, 7, 13559

In situ growth of a POMOF-derived nitride based composite on Cu foam to produce hydrogen with enhanced water dissociation kinetics†

Yu-Jia Tang,‡[ab] Yu Wang,‡[c] Hong-Jing Zhu,[a] Kun Zhou *[bc] and Ya-Qian Lan*[a]

Dispersing active materials on a working electrode without any binder is always desirable for electrocatalytic processes. Here we report a promising method to grow polyoxometalate-based MOFs (POMOFs) *in situ* on a copper foam (CF) substrate. Impressively, CF can serve as metal nodes for the direct growth of MOFs on its 3D skeleton tightly. After ammoniating the POMOFs/CF precursor, a nitride-based composite (MoN–Cu-NPC/CF) is achieved with such a unique structure with MoN and Cu nanoparticles embedded in N, P-doped amorphous carbon and decorated on CF uniformly. We find that MoN–Cu-NPC/CF has an improved HER activity over a wide pH range. Especially in an alkaline electrolyte, this composite shows a small onset overpotential of 60 mV, a Tafel slope of 152 mV dec^{-1} and an outstanding long-term stability (over 20 h), outperforming most of the nitride-based HER electrocatalysts to date. Density functional theory (DFT) calculations reveal that the synergy between MoN and Cu can modify the electronic structure of the active Cu sites, which significantly improves H* binding and water dissociation kinetics. This work provides a facile strategy for *in situ* growth of MOFs on a metal substrate without any binder and holds substantial promise for efficient HER applications.

Received 27th February 2019
Accepted 26th April 2019

DOI: 10.1039/c9ta02200g

rsc.li/materials-a

Introduction

Electrolysis of water to produce gaseous hydrogen (H_2) is a promising technology to meet the growing energy demands. In recent years, numerous research studies have been reported for the exploration of high-performance electrode materials to improve the kinetics of the hydrogen evolution reaction (HER), especially in an alkaline electrolyte.[1,2] Noble metal-based materials are well regarded as state-of-art electrocatalysts towards the HER.[3–5] However, these electrocatalysts are costly and have low abundance, which are not suitable for industrialization. Therefore, non-noble metal-based electrocatalysts with excellent activity and low cost are highly desirable for efficient production of H_2.[6,7] Despite considerable research on these materials, such as transition metal sulphides,[8,9] phosphides,[10,11] carbides[12,13] and heteroatom-doped carbon materials,[14,15] designing and synthesizing efficient HER electrocatalysts remains a great challenge.

Metal–organic frameworks (MOFs) are a type of typical porous crystals with distinguishing features including an adjustable pore size, high surface area and optional metal ions/clusters.[16,17] Calcination of MOF powders provides a feasible method to synthesize porous carbon-confined nanocomposites for renewable energy applications.[18–21] Particularly, MOF-derived nanomaterials have been considered to be the promising commercial Pt/C replacement electrocatalysts for the HER.[22–24] Despite these advantages, carbon-based nanocomposites are inclined to agglomerate to form granular particles by high-temperature carbonization of MOF powders. If MOFs are grown uniformly and tightly on a conductive support (*e.g.*, carbon fiber paper and nickel foam), the problem of derivatives being aggregated can be solved.[25,26] However, MOFs, especially large-sized crystals, directly grown on a substrate through weak van der Waals interactions are likely to fall off, thus decreasing the activity and stability for electrolysis. In this regard, we can choose a specific metal support as metal nodes to grow MOFs tightly and homogenously.[27] For example, a copper foam (CF) substrate can be surface oxidized and used as the metal nodes to grow HKUST-1, which is a well-known MOF assembled from paddlewheel-type Cu(II) nodes and 1,3,5-benzenetricarboxylate (BTC) linkers.[28] Therefore, *in situ* growth of MOFs on a metal substrate can open up a new opportunity for the development of functional electrodes mainly in frontier electrochemical fields.

[a]Jiangsu Collaborative Innovation Centre of Biomedical Functional Materials, Jiangsu Key Laboratory of New Power Batteries, School of Chemistry and Materials Science, Nanjing Normal University, Nanjing 210023, China. E-mail: yqlan@njnu.edu.cn
[b]School of Mechanical and Aerospace Engineering, Nanyang Technological University, 50 Nanyang Avenue, Singapore 639798, Singapore. E-mail: kzhou@ntu.edu.sg
[c]Environmental Process Modelling Centre, Nanyang Environment and Water Research Institute, Nanyang Technological University, 1 CleanTech Loop, Singapore 637141, Singapore

† Electronic supplementary information (ESI) available: SEM, PXRD, XPS, LSV, Tafel, CV, *i–t*, tables and so on. See DOI: 10.1039/c9ta02200g

‡ These authors contributed equally to this work.

Metal nitrides (MNs) have been regarded as effective electrocatalysts in H_2 production recently.[29–31] MNs have a variety of advantages including excellent electronic conductivity, high melting temperature and good mechanical strength. However, pure-phase nitrides usually have high overpotentials and poor corrosion stability in acidic or alkaline electrolytes during electrocatalytic measurements. Notably, porous carbon-confined nitrides can improve the long-term stability and avoid corrosion effectively.[32] Adopting a good method to conduct ammoniation treatment of MOFs can yield the nitride-based nanocomposite with a unique structure.[33,34] Therefore, combining the above concepts, MOFs which are *in situ* grown on a substrate as a precursor can be ammoniated to synthesize a porous carbon-confined nitride-based composite. The as-prepared nitride-based electrocatalysts not only have high surface areas, exposed active sites and a short electronic transmission path but also possess good electronic conductivity and structural stability.

In this work, we have *in situ* grown polyoxometalate-based MOF (POMOF) crystals on a CF substrate (POMOFs/CF) without any binder. The CF substrate was used as both the conductive support and the metal copper nodes to synthesize HKUST-1 crystals. Keggin-type polyoxometalates (POMs) of phosphomolybdic acid (PMo_{12}) with an appropriate size and shape were introduced into the pores of HKUST-1 to synthesize POMOFs (PMo_{12}@HKUST-1).[35,36] Then, a nitride-based composite (MoN–Cu-NPC/CF) was prepared by directly annealing POMOFs/CF in an ammonia (NH_3) atmosphere. Remarkably, MoN–Cu-NPC/CF served as the working electrode for the HER with impressive activity and stability in different electrolytes, surpassing most reported nitride-based HER electrocatalysts to date. Density functional theory (DFT) calculations corroborated that the high activity was fundamentally attributed to the synergistic effect between MoN and Cu, in which the underlying interfacial charge transfer could modify the active Cu sites and hence accelerate the water dissociation kinetics.

Experimental

Chemicals

All chemicals were purchased and used without purification. Ammonium persulfate ($(NH_4)_2S_2O_8$, ≥98.0%), sodium hydroxide (NaOH, 98%), potassium hydroxide (KOH, ≥96%), sulfuric acid (H_2SO_4, 98%), sodium dihydrogen phosphate dihydrate ($NaH_2PO_4 \cdot 2H_2O$, AR), sodium phosphate dibasic anhydrous (Na_2HPO_4, AR), phosphomolybdic acid ($H_3PMo_{12}O_{40} \cdot nH_2O$), and 1,3,5-benzenetricarboxylate (BTC, 98%) were supplied by Sinopharm Chemical Reagent Co., Ltd. 20% Pt/C and Nafion solution (5 wt%) were purchased from Sigma-Aldrich.

Preparation of the PMo_{12}@HKUST-1/CF precursor

First, Cu foam with a size of 1 × 2 cm^2 was washed with water, ethanol and acetone, respectively. $(NH_4)_2S_2O_8$ (5 mmol, 1.14 g) and NaOH (120 mmol, 4.8 g) were dissolved in 50 mL water to form a clear solution. A piece of clean Cu foam was then immersed in the above solution at 80 °C for 20 min to ensure surface oxidation. The oxidized Cu foam was washed with water several times and immersed in water for use. Afterwards, BTC (0.1 mmol, 21 mg) and PMo_{12} (0.02 mmol, 37 mg) were dissolved in a mixture of 5 mL water and 5 mL ethanol by sonication. A piece of oxidized Cu foam was immersed in the above solution and allowed to stand at room temperature for 24 h. Finally, PMo_{12}@HKUST-1/CF was collected by washing with a water/ethanol solution and dried at 60 °C overnight. For comparison, HKUST-1/CF was prepared without adding PMo_{12}.

Preparation of MoN–Cu-NPC/CF

PMo_{12}@HKUST-1/CF was annealed at 400 °C (5 °C min^{-1} heating rate) for 5 h under a NH_3 flow. After cooling to room temperature, MoN–Cu-NPC/CF was obtained with a loading mass of *ca.* 2 mg cm^{-2}. For comparison, Cu-NC/CF was obtained by ammoniation of the HKUST-1/CF precursor.

Material characterization

Powder X-ray diffraction (PXRD) patterns were recorded on a D/max 2500VL/PC diffractometer (Japan) equipped with graphite monochromatized Cu Kα radiation (λ = 1.54060 Å). The corresponding work voltage and current were 40 kV and 100 mA, respectively. Transmission electron microscopy (TEM) and high-resolution TEM (HRTEM) images were obtained on a JEOL-2100F apparatus at an accelerating voltage of 200 kV. Morphology and microstructure analysis was conducted using a scanning electron microscope (SEM, JSM-7600F) at an acceleration voltage of 10 kV. Energy dispersive X-ray spectroscopy (EDS) was performed with a JSM-5160LV-Vantage typed energy spectrometer. X-ray photoelectron spectroscopy (XPS) was carried out on a scanning X-ray microprobe (PHI 5000 Verasa, ULAC-PHI, Inc.) using Al kα radiation and the C 1s peak at 284.8 eV as the internal standard. N_2 adsorption–desorption isotherms were recorded using an Autosorb-iQ (Quantachrome Instruments, U.S.).

Electrochemical measurements

Electrochemical measurements for the HER were performed on an electrochemical workstation (SP-150, Bio-logic) using a typical three-electrode system. MoN–Cu-NPC/CF was used as the direct working electrode. A saturated calomel electrode (SCE) and a graphene rod were used as the reference and counter electrodes, respectively. Electrolytes with different pH values were chosen including 1 M KOH (pH = 14), 0.5 M H_2SO_4 (pH = 0) and 0.5 M PBS (pH = 6.8). Working potentials were converted with respect to the reversible hydrogen electrode (RHE) according to the equation: $E_{RHE} = E_{SCE} + 0.059$ pH. The measurement area was 1 × 1 cm^2. All the polarization curves were corrected using 85% *iR* compensation. Before performing linear sweep voltammetry (LSV) at 5 mV s^{-1}, the cyclic voltammetry (CV) curves were recorded at potentials ranging from −0.2 to 0.2 V *vs.* RHE for 100 cycles at 100 mV s^{-1}. The long-term stability was measured at a constant overpotential for 20 h. The electrochemical impedance spectroscopy (EIS) spectra were recorded at an overpotential of 200 mV in the frequency range

from 1000 kHz to 10 mHz with an amplitude of 10 mV. The electrochemical double-layer capacitance (C_{dl}) was calculated from the CV curves tested in a non-faradaic region (−0.8 to −0.7 V *vs.* SCE) at different scan rates (10, 20, 40, 60, 80, and 100 mV s^{-1}) in 1 M KOH. In contrast, 10 mg commercial 20% Pt/C was dispersed into 1 mL solution containing 0.1 mL Nafion (5 wt%) and 0.9 mL water. The above mixture was dropped onto Cu foam with a loading mass of 2 mg cm^{-2}.

Computational methods

DFT calculations were performed using the revised Perdew–Burke–Ernzerhof generalized gradient approximation exchange–correlation functional[37] and the projector-augmented plane wave approach,[38,39] as implemented in the VASP code.[40,41] For all structure optimizations, a plane-wave cutoff energy of 420 eV was employed with a Methfessel–Paxton smearing width of 0.1 eV and a *k*-point sampling of ~0.04 $Å^{-1}$. The convergence threshold of energy was 4×10^{-5} eV, and that of force on each ion was 0.01 eV $Å^{-1}$. Denser *k*-point sampling (~0.02 $Å^{-1}$) was utilized in electronic structure calculations. The transition state (TS) of water dissociation was identified using the climbing-image nudged elastic band (CI-NEB) technique,[42] and was confirmed by vibrational frequency analysis (only one imaginary frequency). The details of models and free energy calculations are provided in the ESI.†

Results and discussion

The synthesis process of MoN–Cu-NPC/CF involved three steps, as illustrated in Fig. 1. First, CF with a size of 1×2 cm^2 was oxidized using the mixed solution of $(NH_4)_2S_2O_8$ and NaOH as the oxidant. Second, the partially oxidized CF was immersed in PMo_{12} and BTC solution. After standing at room temperature for 24 h, deep-green octahedral crystals on CF (PMo_{12}@HKUST-1/CF) could be obtained. Last, NH_3 was used as the N source to anneal PMo_{12}@HKUST-1/CF at 400 °C for 5 h to obtain the nitride-based composite with black colour (MoN–Cu-NPC/CF) (Fig. 2a). For comparison, HKUST-1/CF and the derived Cu-NC/CF were synthesized without PMo_{12} (details are given in the Experimental section).

The compositions of the samples were characterized by powder X-ray diffraction (PXRD). The PXRD spectrum of the oxidized CF shows that the diffraction peaks could be indexed to the simulated patterns of Cu (JCPDS no. 1-1242) and CuO (JCPDS no. 5-661), suggesting partial surface oxidization of Cu to CuO (Fig. S1†). The diffraction peaks of PMo_{12}@HKUST-1/CF and HKUST-1/CF were in accordance with the corresponding simulated patterns, demonstrating the successful synthesis of MOFs (Fig. 2b). Fig. S2† shows the PXRD spectra of MoN–Cu-NPC/CF prepared at different annealing temperatures (400, 600 and 800 °C). The peak intensity became strong as the ammoniation temperature increased. The typical peaks with a high intensity at 43.5, 50.8, and 74.6° were assigned to Cu and are in agreement with JCPDS no. 1-1242. Other characteristic peaks at 32.0, 36.3, 49.0, and 65.1° were consistent with the simulated MoN diffraction pattern (JCPDS no. 25-1367).[43] In addition, the PXRD pattern of MoN–Cu-NPC/CF prepared at 400 °C exhibited a weak peak at 36.3°, demonstrating the low crystallization degree of MoN.

In order to observe the morphologies of the relevant samples, scanning electron microscopy (SEM) images were taken. The SEM images in Fig. S3† shows that the CF substrate possessed a 3D skeleton with a smooth surface. In comparison, the surface of the oxidized CF became rough due to the formation of CuO nanosheets (Fig. 2c). PMo_{12}@HKUST-1/CF showed micron-sized crystals with an octahedral morphology and a smooth surface grown on the CF skeleton compactly (Fig. 2d). After the ammoniation treatment of the POMOFs/CF precursor, the as-prepared MoN–Cu-NPC/CF became surface wrinkled but still preserved the octahedral morphology (Fig. 2e and f). By contrast, HKUST-1/CF showed small-sized crystals on

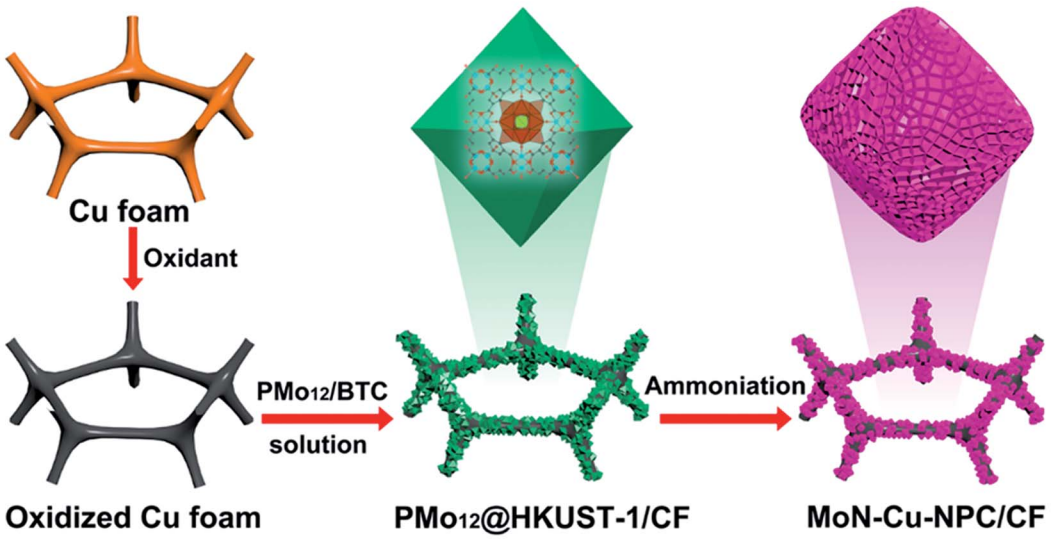

Fig. 1 Schematic illustration for the synthesis of MoN–Cu-NPC/CF.

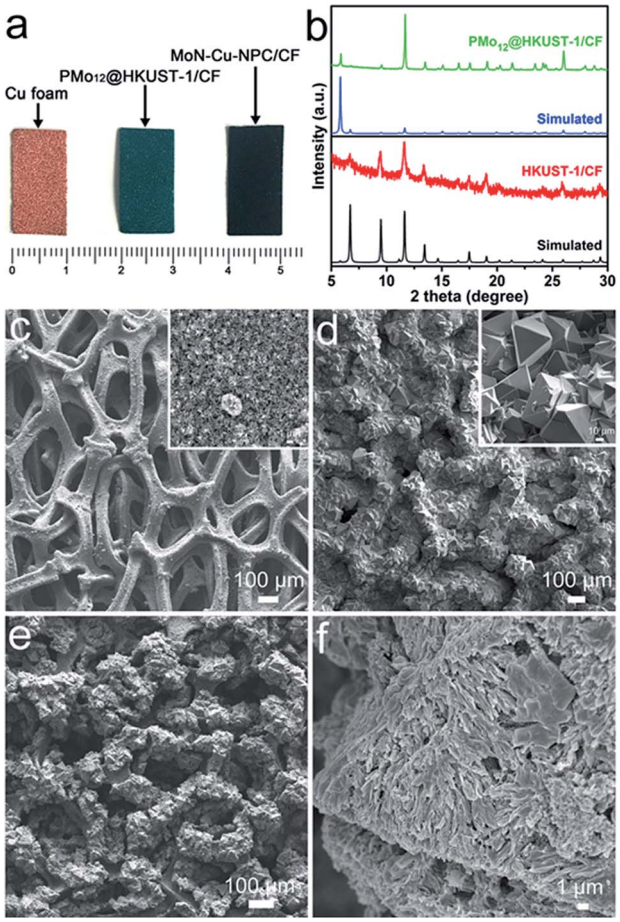

Fig. 2 (a) Photograph of CF, PMo_{12}@HKUST-1/CF and MoN–Cu-NPC/CF with a size of 1 × 2 cm^2. (b) PXRD spectra of PMo_{12}@HKUST-1/CF and HKUST-1/CF as well as the simulated patterns. SEM images: (c) oxidized Cu foam with the inset being the partial enlarged image; (d) PMo_{12}@HKUST-1/CF with the inset being the partial enlarged image; (e and f) MoN–Cu-NPC/CF at different scales.

CF, suggesting that the introduction of POMs into pores had an important influence on the particle size difference between PMo_{12}@HKUST-1 and HKUST-1 (Fig. S4a and b†). However, the octahedral morphology of Cu-NC/CF was destroyed, which displayed Cu-NC particles with uneven sizes attached to the CF surface separately (Fig. S4c and d†). Moreover, Fig. S5 and S6† show the PXRD and SEM characterization at different time intervals to study the minute changes and observations for the preparation process of MoN–Cu-NPC/CF.

The transmission electron microscopy (TEM) image of MoN–Cu-NPC sonicated from the CF substrate is shown in Fig. 3a. The nano-sized metal particles of MoN and Cu were dispersed in porous carbon. The lattices of MoN and Cu can be observed in the high-resolution TEM (HRTEM) images (Fig. 3b). A lattice spacing of 0.208 nm corresponds to the (111) plane of Cu. The lattice fringes at the edge of the metal particles displayed a lattice spacing of 0.247 nm, which was assigned to the (200) plane of MoN. The porous carbon around the metal particles was amorphous due to the relatively low ammoniation temperature. The energy dispersive X-ray (EDX) spectrum of MoN–Cu-NPC/CF demonstrates the existence of all elements including C, N, O, P, Mo and Cu (Fig. 3c). The high-angle annular dark field (HAADF) image and the corresponding element mappings of MoN–Cu-NPC show that Mo and Cu elements were concentrated in the bright particle area while N, P and C elements were uniformly distributed in the whole sample (Fig. 3d). All these results suggest that MoN–Cu-NPC had a special structure with MoN–Cu nanoparticles embedded in N, P-doped amorphous porous carbon. In addition, the porous structure of MoN–Cu-NPC/CF was determined from the nitrogen (N_2) adsorption–desorption isotherm (Fig. S7†). MoN–Cu-NPC/CF had a Brunauer–Emmett–Teller (BET) surface area of 11.3 $m^2\ g^{-1}$ and contained mesopores mainly in the range from 2.5 to 18 nm as analyzed through quenched solid density functional theory (QSDFT) analysis.

X-ray photoelectron spectroscopy (XPS) was applied to analyze the chemical valence on the surface of the sample. The high-resolution Cu 2p XPS spectrum proves the partial oxidation of the CF substrate to form CuO nanosheets (Fig. S8†). Fig. 4a shows the full-scan spectrum of MoN–Cu-NPC/CF with sharp peaks for all existing elements. The atomic percentage of the corresponding elements analyzed through XPS is shown in Table S1.† The high-resolution Mo 3d spectrum exhibits two different valence states (Fig. 4b). The binding energies at 235.2 and 233.3 eV were ascribed to Mo^{6+} $3d_{3/2}$ and Mo^{6+} $3d_{5/2}$, while two peaks at 232.3 and 230.4 eV were assigned to Mo^{4+} $3d_{3/2}$ and Mo^{4+} $3d_{5/2}$. Additionally, the peak at 229.4 eV belonged to the Mo–N bond, indicating the successful preparation of MoN.[44] The Cu 2p spectrum presents two main regions including Cu $2p_{1/2}$ and Cu $2p_{3/2}$ (Fig. 4c). In the Cu $2p_{1/2}$ region, there are two peaks located at 954.1 and 952.4 eV corresponding to the Cu(II) and Cu(0) species, respectively. Similarly, the Cu $2p_{3/2}$ region shows the surface compositions of Cu(II) at 934.4 eV and Cu(0) at 932.6 eV. However, the binding energies of Cu(I) and Cu(0) were very close in the Cu $2p_{3/2}$ region, which could not be distinguished by XPS.[45,46] Cu_2O was usually formed by high-temperature annealing and could not be synthesized at a low ammoniation temperature (400 °C). The PXRD pattern of MoN–Cu-NPC/CF also proves no evidence of Cu_2O. Therefore, the existence of Cu(II) resulted from the partial surface oxidation of MoN–Cu-NPC/CF when it was exposed in air or the CuO did not coordinate with the BTC ligands. The Cu(0) species was derived from the CF substrate. The other two peaks at 962.5 and 942.7 eV can be indexed to the satellite peaks. The N 1s spectrum possesses two main peaks at 399.4 and 398.3 eV, which are assigned to pyrrolic N and pyridinic N, respectively (Fig. 4d). Another peak at 396.5 eV corresponds to the Mo–N bond, which is the typical peak of MNs. The P 2p spectrum in Fig. 4e displays the peak for P–O species, indicating P doping in MoN–Cu-NPC/CF. The C 1s spectrum can be deconvoluted into four peaks, which were C–C/C=C (284.6 eV), C–N/C–O (285.4 eV), C=O (286.4 eV) and O–C=O (289.2 eV), respectively (Fig. 4f). The main peak at 284.6 eV came from carbon in the MoN–Cu-NPC composite because of the abundant carbon sources derived from BTC linkers. All these XPS results evidenced the successful synthesis of the MoN–Cu-NPC/CF composite.

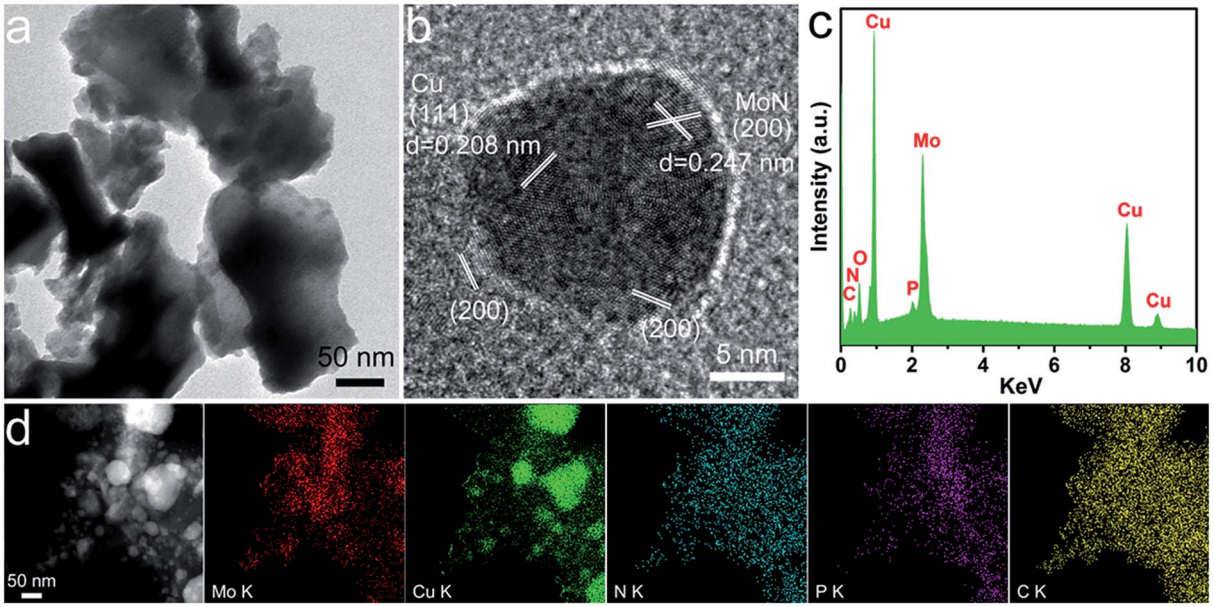

Fig. 3 Structural characterization of MoN–Cu-NPC sonicated from the CF substrate: (a) TEM image, (b) HRTEM image, (c) EDX spectrum and (d) HAADF image and the corresponding element mappings.

In order to determine the effect of the samples prepared with and without POMs in the precursor, the electrocatalytic performance for the HER was investigated in electrolytes with different pH values using a typical three-electrode system. The samples including MoN–Cu-NPC/CF, Cu-NC/CF, CF and commercial 20% Pt/C coated on CF were used as the working electrodes and measured for comparison. Fig. 5a shows the liner sweep voltammetry (LSV) curves of four samples measured in 1 M KOH. MoN–Cu-NPC/CF exhibited a lower onset overpotential (*ca.* 60 mV) and a higher current density than the other samples except 20% Pt/C on CF with an onset overpotential of 0 mV. Moreover, a small overpotential of 127 mV was required for MoN–Cu-NPC/CF to reach a current density of 10 mA cm^{-2} (η_{10}), which was much smaller than those of Cu-NC/CF (209 mV) and CF (460 mV). Similarly, the LSV curves measured in other electrolytes including 0.5 M H_2SO_4 and 0.5 M PBS are shown in Fig. S9a and b.† MoN–Cu-NPC/CF possessed smaller η_{10} values of 188 and 158 mV than those of Cu-NC/CF and CF in acidic and neutral electrolytes, respectively.

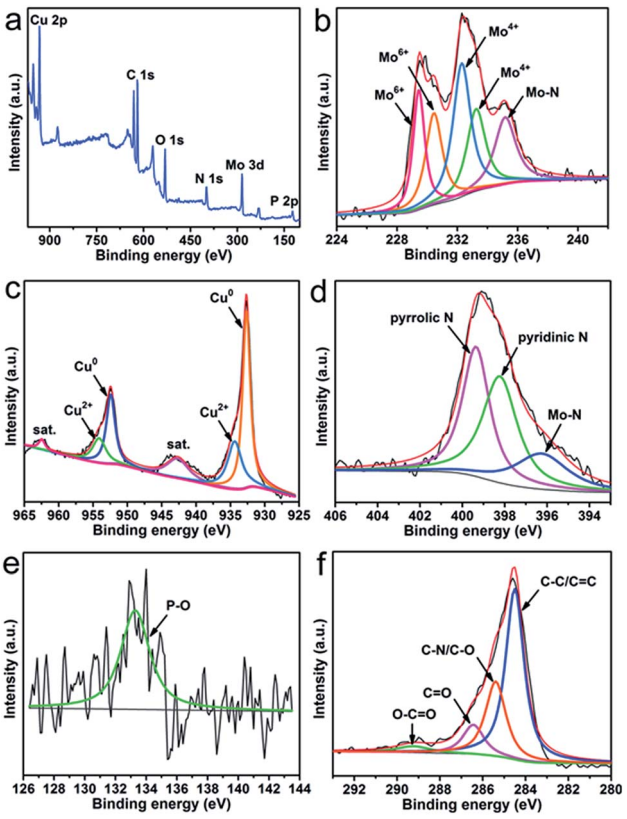

Fig. 4 XPS spectra of MoN–Cu-NPC/CF: (a) full-scan, (b) Mo 3d, (c) Cu 2p, (d) N 1s, (e) P 2p and (f) C 1s.

Tafel plots (η *vs.* log j) were obtained to further confirm the HER activity (Fig. 5b). In 1 M KOH, MoN–Cu-NPC/CF had a small Tafel slope of 152 mV dec^{-1} compared with Cu-NC/CF (179 mV dec^{-1}), CF (344 mV dec^{-1}) and commercial 20% Pt/C (55 mV dec^{-1}), suggesting the enhanced HER kinetic electroactivity. In addition, the calculated Tafel slopes of MoN–Cu-NPC/CF in acidic and neutral electrolytes were 144 and 203 mV dec^{-1}, respectively (Fig. S9c and d†). Such low η_{10} and Tafel slopes of MoN–Cu-NPC/CF achieved in different electrolytes were superior to those of most reported non-noble metal-based HER electrocatalysts, such as γ-Mo_2N,[47] WN NW,[48] Co–Ni_3N,[49] NiS_2/MoS_2 HNW[50] and FeP NPs@NPC[51] (Table S2†).

To verify the long-term stability of MoN–Cu-NPC/CF, the LSV curves before and after 2000 cyclic voltammetry (CV) cycles measured in 1 M KOH are shown in Fig. 5c. There was no current density degradation after long-term cycling, suggesting the excellent electrocatalytic stability of the MoN–Cu-NPC/CF

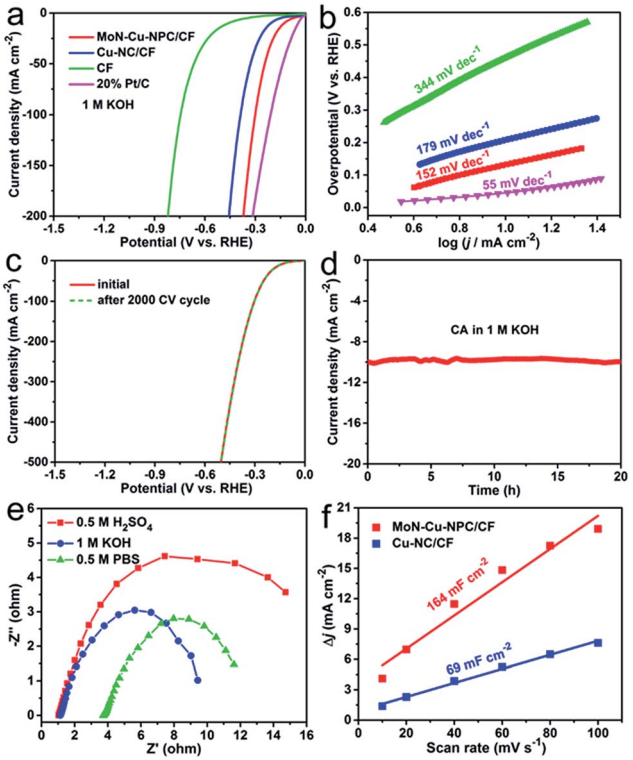

Fig. 5 (a) LSV curves of MoN–Cu-NPC/CF, Cu-NC/CF, CF and commercial 20% Pt/C in 1 M KOH at 5 mV s^{-1}. (b) Corresponding Tafel plots. (c) LSV curves of MoN–Cu-NPC/CF initially and after 2000 CV cycles. (d) CA curve of MoN–Cu-NPC/CF recorded at a constant overpotential for 20 h in 1 M KOH. (e) EIS spectrum of MoN–Cu-NPC/CF recorded at an overpotential of 200 mV in three different electrolytes. (f) Current density difference (j_a–j_c) *vs.* scan rate plots of MoN–Cu-NPC/CF and Cu-NPC/CF.

electrode. Chronoamperometry (CA) curves were also recorded at a constant overpotential for 20 h in different electrolytes. For example, the CA curve measured at an overpotential of 130 mV in 1 M KOH shows no decrease in the current density at 10 mA cm^{-2}, suggesting its enhanced electrocatalytic stability in a harsh medium (Fig. 5d). In contrast, the CA curves obtained in acidic and neutral electrolytes show 85% and 96% of the current density after 20 h of cycling, respectively (Fig. S10†). Apparently, MoN–Cu-NPC/CF had a better HER performance than Cu-NC/CF, which could be attributed to the unique structure of the POMOF precursor and the POMOF-derived nitride-based composite. Furthermore, a series of post characterization studies (*i.e.*, PXRD, SEM and XPS) were applied to study the composition and morphology of MoN–Cu-NPC/CF after the stability test in electrolytes with different pH values (Fig. S11–13†).

Electrochemical impedance spectroscopy (EIS) was used to estimate the electron transfer ability at the solid/electrolyte interface. The EIS spectra of MoN–Cu-NPC/CF in all-pH-values electrolytes all show small semicircles in the high-frequency region (Fig. 5e). The charge transfer resistance R_{ct} in alkaline, acidic, and neutral media was 8.2, 12.4 and 8.7 Ω, respectively, confirming the fast kinetics of MoN–Cu-NPC/CF. Moreover, the electrochemical surface area (ESCA) could provide an insight into the HER activity, which was related to the electrochemical double-layer capacitance C_{dl}. The C_{dl} was the slope of the capacitive current density difference (j_a–j_c) against the different scan rates. Fig. S14† shows the CV curves of MoN–Cu-NPC/CF and Cu-NC/CF measured in a non-faradaic region in an alkaline medium. According to the slope calculation in Fig. 5f, MoN–Cu-NPC/CF exhibited a large C_{dl} of 164 mF cm^{-2}, which was more than two-fold that of Cu-NC/CF (69 mF cm^{-2}). Therefore, MoN–Cu-NPC/CF had a low R_{ct} and a large ECSA because of the unique porous structure and exposed active sites, leading to excellent HER properties.

In contrast, the increase of the ammoniation temperature led to an obvious decrease of HER performance in an alkaline electrolyte. According to LSV curves in Fig. S15,† the η_{10} values of MoN–Cu-NPC/CF synthesized at 600 and 800 °C were 205 and 260 mV, respectively, which were higher than those of the sample prepared at 400 °C. In addition, different POM loadings in the pores of HKUST-1 were analyzed. The PXRD spectra of PMo_{12}@HKUST-1/CF with less (20 mg) and more (80 mg) POM loadings were in accordance with the simulated pattern, demonstrating the successful synthesis of POMOFs/CF (Fig. S16†). MoN–Cu-NPC/CF with different Mo loadings exhibited different HER performance (Fig. S17†). MoN–Cu-NPC/CF prepared using 40 mg POMs in solution had the best electrocatalytic activity for the HER in an alkaline electrolyte.

A series of first-principles DFT calculations were performed to study the activity origin of MoN–Cu-NPC/CF toward the HER in alkaline solutions. Here, three independent periodic surface slabs, including the Cu (111), MoN (001), and hybrid MoN–Cu planes, were constructed to represent the active surfaces in MoN–Cu-NPC/CF and Cu-NC/CF. We compared the free energy for H* adsorption (ΔG_{H^*}), as the Sabatier principle had established an optimal value for H* binding ($\Delta G_{H^*} \approx 0$ eV).[52] The optimized geometric structures of H* adsorbed on the slabs are shown in Fig. S18.† The calculated free energy diagram demonstrated a relatively weak H* adsorption in pristine Cu ($\Delta G_{H^*} = 0.21$ eV) and a strong H* binding for MoN alone ($\Delta G_{H^*} = -0.66$ eV), both of which were far away from the ideal value, suggesting that Cu or MoN alone were intrinsically inactive for the HER (Fig. 6a). Notably, when Cu was supported on MoN, the H* binding on the Cu sites of the hybrid MoN–Cu was significantly enhanced to $\Delta G_{H^*} = 0.07$ eV; while as a reference, Pt had a favorable value of −0.09 eV, implying that the synergistic MoN and Cu could optimize H* adsorption to boost the HER process.

To gain an intuitive understanding on the synergistic effect-driven improvement of H* adsorption on MoN–Cu, the interfacial electron transfer between Cu and MoN is shown in Fig. 6b. From the charge density difference, a considerable electron transfer from both Mo and Cu to the MoN–Cu interface could be found, yielding electron depletion regions on the Mo atoms and the outer Cu sites. Theoretically, such electron-deficient Cu sites could provide more empty orbitals to bond with the H atom, hence enhancing H* adsorption. This difference in the electronic and adsorption characteristics of Cu sites in pristine Cu and MoN–Cu could be inferred from their electronic density of states (DOS), in which the position of the

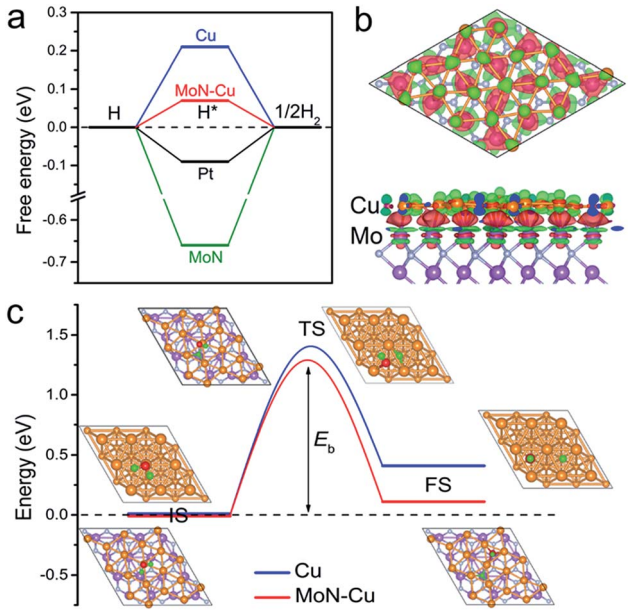

Fig. 6 (a) Calculated ΔG_{H^*} of MoN, Cu, MoN–Cu, and the Pt reference. (b) Top and side views of electron transfer in MoN–Cu. Red and green colours denote electron accumulation and depletion regions, respectively. The iso-surface value is 0.004 e Å^{-3}. (c) Calculated energy diagram of water dissociation on Cu and MoN–Cu slabs. The insets are the atomic configurations of the initial state (IS), transition state (TS), and final state (FS). Cu, Mo, N, O, and H are represented as orange, purple, gray, red, and green spheres, respectively.

energy level featuring the highest states, E_p, was regarded as a good descriptor.[53,54] Generally, with E_p closer to the Fermi level E_f, the antibonding states of the system moved higher with a lower occupancy, which potentially resulted in stronger adsorption to the adsorbate. As expected, the projected DOS of Cu-3d showed that the E_p of MoN–Cu was closer to E_f than that of pristine Cu, in agreement with the order of H* adsorption strength (Fig. S19†).

Since the alkaline HER processes were intrinsically governed by the kinetics of H* formation from water dissociation,[55] the climbing-image nudged elastic band (CI-NEB) methodology was used to explore the transition state and energy barrier E_b of the water dissociation process. According to the CI-NEB calculations, the E_b for water dissociation on Cu was identified to be 1.40 eV (Fig. 6c). Remarkably, with the support of MoN, the E_b was reduced to 1.29 eV, indicating that synergistic MoN and Cu could improve water dissociation kinetics. Therefore, MoN–Cu-NPC/CF exhibited excellent alkaline HER performance. Overall, both the experimental and theoretical results indicated that MoN–Cu-NPC/CF is a promising and highly efficient electrocatalyst for the HER in an alkaline electrolyte.

Conclusions

In conclusion, we have presented a novel method to synthesize PMo_{12}@HKUST-1 crystals *in situ* on a CF substrate as well as the derived MoN–Cu-NPC/CF composite. The CuO nanosheets on CF as the metal nodes ensured the uniform epitaxial growth of POMOFs on its 3D skeleton. After POMOFs/CF was ammoniated, MoN–Cu-NPC/CF exhibited a unique structure with MoN and Cu nanoparticles dispersed in N, P-doped amorphous carbon and decorated on CF uniformly. The high HER performance of MoN–Cu-NPC/CF was achieved with a low η_{10} of 127 mV, a Tafel slope of 152 mV dec^{-1} and a long-term stability (over 20 h) in an alkaline electrolyte due to the synergistic effect of MoN and Cu confined in carbon. DFT calculations demonstrated that the significant electron transfer from MoN and Cu to the MoN–Cu interface could yield active electron-deficient Cu sites, thus improving the H* binding and kinetics of H* formation from water dissociation. Based on the scalability and feasibility, this work will lead to a facile strategy for the growth of MOFs on a conductive substrate that can provide metal nodes directly, thus serving as a high-performance electrode for water splitting, metal–air batteries and other electrocatalytic reactions.

Conflicts of interest

There are no conflicts to declare.

Acknowledgements

This work is financially supported by the NSFC (No. 21622104, 21871141, 21871142 and 21701085), the NSF of Jiangsu Province of China (No. SBK2017040708), the Natural Science Research of Jiangsu Higher Education Institutions of China (No. 17KJB150025), the Priority Academic Program Development of Jiangsu Higher Education Institutions and the Foundation of Jiangsu Collaborative Innovation Center of Biomedical Functional Materials. The authors acknowledge the financial support from the Nanyang Environment and Water Research Institute (CoreFund), Nanyang Technological University, Singapore.

Notes and references

1 M. S. Dresselhaus and I. L. Thomas, *Nature*, 2001, **414**, 332–337.
2 J. A. Turner, *Science*, 2004, **305**, 972–974.
3 C. C. L. McCrory, S. Jung, I. M. Ferrer, S. M. Chatman, J. C. Peters and T. F. Jaramillo, *J. Am. Chem. Soc.*, 2015, **137**, 4347–4357.
4 W. Sheng, H. A. Gasteiger and Y. Shao-Horn, *J. Electrochem. Soc.*, 2010, **157**, B1529–B1536.
5 Y. Liu, S. Liu, Y. Wang, Q. Zhang, L. Gu, S. Zhao, D. Xu, Y. Li, J. Bao and Z. Dai, *J. Am. Chem. Soc.*, 2018, **140**, 2731–2734.
6 S. Anantharaj, S. R. Ede, K. Sakthikumar, K. Karthick, S. Mishra and S. Kundu, *ACS Catal.*, 2016, **6**, 8069–8097.
7 Y. Jiao, Y. Zheng, M. Jaroniec and S. Z. Qiao, *Chem. Soc. Rev.*, 2015, **44**, 2060–2086.
8 C. G. Morales-Guio and X. Hu, *Acc. Chem. Res.*, 2014, **47**, 2671–2681.
9 X. Zou, Y. Liu, G.-D. Li, Y. Wu, D.-P. Liu, W. Li, H.-W. Li, D. Wang, Y. Zhang and X. Zou, *Adv. Mater.*, 2017, **29**, 1700404.

10 T. Liu, A. Li, C. Wang, W. Zhou, S. Liu and L. Guo, *Adv. Mater.*, 2018, **30**, 1803590.
11 S.-H. Yu, R. Wu, B. Xiao, Q. Gao, Y. Zheng, X. Zheng, J. Zhu and M.-R. Gao, *Angew. Chem., Int. Ed.*, 2018, **130**, 15671–15675.
12 H. Lin, N. Liu, Z. Shi, Y. Guo, Y. Tang and Q. Gao, *Adv. Funct. Mater.*, 2016, **26**, 5590–5598.
13 P. Xiao, X. Ge, H. Wang, Z. Liu, A. Fisher and X. Wang, *Adv. Funct. Mater.*, 2015, **25**, 1520–1526.
14 C. Hu and L. Dai, *Adv. Mater.*, 2017, **29**, 1604942.
15 Y. Zhang, X. Xia, X. Cao, B. Zhang, N. H. Tiep, H. He, S. Chen, Y. Huang and H. J. Fan, *Adv. Energy Mater.*, 2017, **7**, 1700220.
16 H. Wang, Q.-L. Zhu, R. Zou and Q. Xu, *Chem*, 2017, **2**, 52–80.
17 H. Furukawa, K. E. Cordova, M. O'Keeffe and O. M. Yaghi, *Science*, 2013, **341**, 1230444.
18 H. Zhang, X. Liu, Y. Wu, C. Guan, A. K. Cheetham and J. Wang, *Chem. Commun.*, 2018, **54**, 5268–5288.
19 B. Zhu, D. Xia and R. Zou, *Coord. Chem. Rev.*, 2018, **376**, 430–448.
20 P.-Q. Liao, J.-Q. Shen and J.-P. Zhang, *Coord. Chem. Rev.*, 2017, **373**, 22–48.
21 R. Wu, D. P. Wang, X. Rui, B. Liu, K. Zhou, A. W. K. Law, Q. Yan, J. Wei and Z. Chen, *Adv. Mater.*, 2015, **27**, 3038–3044.
22 W. Chen, J. Pei, C.-T. He, J. Wan, H. Ren, Y. Wang, J. Dong, K. Wu, W.-C. Cheong, J. Mao, X. Zheng, W. Yan, Z. Zhuang, C. Chen, Q. Peng, D. Wang and Y. Li, *Adv. Mater.*, 2018, **30**, 1800396.
23 B. Weng, C. R. Grice, W. Meng, L. Guan, F. Xu, Y. Yu, C. Wang, D. Zhao and Y. Yan, *ACS Energy Lett.*, 2018, **3**, 1434–1442.
24 Y.-J. Tang, M.-R. Gao, C.-H. Liu, S.-L. Li, H.-L. Jiang, Y.-Q. Lan, M. Han and S.-H. Yu, *Angew. Chem., Int. Ed.*, 2015, **54**, 12928–12932.
25 X. F. Lu, L. F. Gu, J. W. Wang, J. X. Wu, P. Q. Liao and G. R. Li, *Adv. Mater.*, 2017, **29**, 1604437.
26 C. Sun, Q. Dong, J. Yang, Z. Dai, J. Lin, P. Chen, W. Huang and X. Dong, *Nano Res.*, 2016, **9**, 2234–2243.
27 G. Cai, W. Zhang, L. Jiao, S.-H. Yu and H.-L. Jiang, *Chem*, 2017, **2**, 791–802.
28 S. S.-Y. Chui, S. M.-F. Lo, J. P. H. Charmant, A. G. Orpen and I. D. Williams, *Science*, 1999, **283**, 1148–1150.
29 N. Han, P. Liu, J. Jiang, L. Ai, Z. Shao and S. Liu, *J. Mater. Chem. A*, 2018, **6**, 19912–19933.
30 W.-F. Chen, J. T. Muckerman and E. Fujita, *Chem. Commun.*, 2013, **49**, 8896–8909.
31 X. Jia, Y. Zhao, G. Chen, L. Shang, R. Shi, X. Kang, G. I. Waterhouse, L. Z. Wu, C. H. Tung and T. Zhang, *Adv. Energy Mater.*, 2016, **6**, 1502585.
32 W.-F. Chen, K. Sasaki, C. Ma, A. I. Frenkel, N. Marinkovic, J. T. Muckerman, Y. Zhu and R. R. Adzic, *Angew. Chem., Int. Ed.*, 2012, **51**, 6131–6135.
33 X. Shi, A. Wu, H. Yan, L. Zhang, C. Tian, L. Wang and H. Fu, *J. Mater. Chem. A*, 2018, **6**, 20100–20109.
34 Y. Zhu, G. Chen, X. Xu, G. Yang, M. Liu and Z. Shao, *ACS Catal.*, 2017, **7**, 3540–3547.
35 D.-L. Long, R. Tsunashima and L. Cronin, *Angew. Chem., Int. Ed.*, 2010, **49**, 1736–1758.
36 C.-Y. Sun, S.-X. Liu, D.-D. Liang, K.-Z. Shao, Y.-H. Ren and Z.-M. Su, *J. Am. Chem. Soc.*, 2009, **131**, 1883–1888.
37 B. Hammer, L. B. Hansen and J. K. Nørskov, *Phys. Rev. B*, 1999, **59**, 7413.
38 P. E. Blöchl, *Phys. Rev. B*, 1994, **50**, 17953.
39 G. Kresse and D. Joubert, *Phys. Rev. B*, 1999, **59**, 1758.
40 G. Kresse and J. Hafner, *Phys. Rev. B*, 1993, **47**, 558.
41 G. Kresse and J. Furthmüller, *Comput. Mater. Sci.*, 1996, **6**, 15–50.
42 G. Henkelman, B. P. Uberuaga and H. Jónsson, *J. Chem. Phys.*, 2000, **113**, 9901–9904.
43 J. Xie, S. Li, X. Zhang, J. Zhang, R. Wang, H. Zhang, B. Pan and Y. Xie, *Chem. Sci.*, 2014, **5**, 4615–4620.
44 Y. Zhang, B. Ouyang, J. Xu, S. Chen, R. S. Rawat and H. J. Fan, *Adv. Energy Mater.*, 2016, **6**, 1600221.
45 Y. Mao, J. He, X. Sun, W. Li, X. Lu, J. Gan, Z. Liu, L. Gong, J. Chen and P. Liu, *Electrochim. Acta*, 2012, **62**, 1–7.
46 M. C. Biesinger, L. W. Lau, A. R. Gerson and R. S. C. Smart, *Appl. Surf. Sci.*, 2010, **257**, 887–898.
47 L. Ma, L. R. L. Ting, V. Molinari, C. Giordano and B. S. Yeo, *J. Mater. Chem. A*, 2015, **3**, 8361–8368.
48 B. Ren, D. Li, Q. Jin, H. Cui and C. Wang, *J. Mater. Chem. A*, 2017, **5**, 19072–19078.
49 C. Zhu, A. L. Wang, W. Xiao, D. Chao, X. Zhang, N. H. Tiep, S. Chen, J. Kang, X. Wang and J. Ding, *Adv. Mater.*, 2018, **30**, 1705516.
50 P. Kuang, T. Tong, K. Fan and J. Yu, *ACS Catal.*, 2017, **7**, 6179–6187.
51 Z. Pu, I. S. Amiinu, C. Zhang, M. Wang, Z. Kou and S. Mu, *Nanoscale*, 2017, **9**, 3555–3560.
52 J. K. Nørskov, T. Bligaard, A. Logadottir, J. Kitchin, J. G. Chen, S. Pandelov and U. Stimming, *J. Electrochem. Soc.*, 2005, **152**, J23–J26.
53 Y. Jiao, Y. Zheng, K. Davey and S.-Z. Qiao, *Nat. Energy*, 2016, **1**, 16130.
54 N. Han, Y. Wang, H. Yang, J. Deng, J. Wu, Y. Li and Y. Li, *Nat. Commun.*, 2018, **9**, 1320.
55 Y. Zheng, Y. Jiao, A. Vasileff and S. Z. Qiao, *Angew. Chem., Int. Ed.*, 2018, **57**, 7568–7579.

